



Materials  
Horizons

**The Energy Landscape Governs Ductility in Disordered  
Materials**

Journal:	<i>Materials Horizons</i>
Manuscript ID	MH-COM-06-2020-000980.R1
Article Type:	Communication
Date Submitted by the Author:	17-Dec-2020
Complete List of Authors:	Tang, Longwen; UCLA LIU, HAN; University of California Los Angeles, Ma, Gang; Wuhan University Du, Tao; Harbin Institute of Technology, Mousseau, Normand; Université de Montréal Zhou, Wei; Wuhan University Bauchy, M.; UCLA

SCHOLARONE™  
Manuscripts

## **New Concept**

When subjected to load, non-crystalline materials can exhibit strikingly different responses, i.e., they can catastrophically break in a brittle fashion or exhibit some ductility. Understanding the nature of the atomic-scale mechanism that governs the propensity for a disordered phase to break in a brittle or ductile fashion has been a longstanding interest in materials science. Here, we investigate numerically the fracture of several archetypal disordered materials. As a major outcome of this work, we reveal for the first time that the degree of ductility during fracture is quantitatively encoded in the topography of the static energy landscape before loading. Our results shed light on intriguing commonalities in the fracture of disordered phases over different material families, microscopic interactions, and scales. This new finding could guide the design of novel noncrystalline phases with unusual resistance to fracture.

Cite this: DOI: 00.0000/xxxxxxxxxx

# The Energy Landscape Governs Ductility in Disordered Materials<sup>†</sup>

Longwen Tang,<sup>ab</sup> Han Liu,<sup>b</sup> Gang Ma,<sup>a</sup> Tao Du,<sup>bc</sup> Normand Mousseau,<sup>d</sup> Wei Zhou,<sup>\*a</sup> and Mathieu Bauchy<sup>\*b</sup>

Received Date

Accepted Date

DOI: 00.0000/xxxxxxxxxx

**Based on their structure, non-crystalline phases can fail in a brittle or ductile fashion. However, the nature of the link between structure and propensity for ductility in disordered materials has remained elusive. Here, based on molecular dynamics simulations of colloidal gels and silica glasses, we investigate how the degree of structural disorder affects the fracture of disordered materials. As expected, we observe that structural disorder results in an increase in ductility. By applying the activation-relaxation technique (an open-ended saddle point search algorithm), we demonstrate that the propensity for ductility is controlled by the topography of the energy landscape. Interestingly, we observe a power-law relationship between the particle non-affine displacement upon fracture and the average local energy barrier. This reveals that the dynamics of the particles upon fracture is encoded in the static energy landscape, i.e., before any load is applied. This relationship is shown to apply to several classes of non-crystalline materials (oxide and metallic glasses, amorphous solid, and colloidal gels), which suggests that it may be a generic feature of disordered materials.**

## 1 Introduction

Understanding the fracture mechanism and dynamics of materials upon fracture is of great importance in materials science

and condensed matter physics<sup>1–3</sup>. Materials can exhibit various mechanisms of fracture, namely, brittle materials fail in a catastrophic fashion within the macroscopic elastic regime, whereas ductile materials feature some irreversible plastic deformation before breaking—thereby reaching high fracture toughness values<sup>4,5</sup>. Select phases have been shown to exhibit some ductile-to-brittle transitions (DBTs), which can be driven by composition<sup>5–7</sup>, thermal history<sup>8,9</sup>, temperature<sup>10</sup>, or loading rate<sup>11,12</sup>.

In crystalline phases, DBTs have been described as a competition between bond-breaking and dislocations<sup>4,13</sup>. However, the origin of DBTs in non-crystalline phases remains less understood<sup>14–18</sup>. The carriers of ductility in disordered materials consist in some local structural reorganizations known as the shear transformation zones (STZs), which have been found to be controlled by the existence of low-frequency vibrational modes<sup>19</sup>, the local "softness" of the structure<sup>20</sup>, the local yield stress<sup>21</sup>, some topological defects<sup>22</sup>, or the local stress gradient<sup>23</sup>. Although previous results suggest the existence of a correlation between STZs and structural/dynamical descriptors<sup>1</sup>, the physical origin of DBTs in disordered materials remains unknown. As an alternative viewpoint, it has been suggested that some mechanical behaviors of glassy materials can be understood based on the energy landscape framework<sup>24</sup>.

Here, we explore whether the degree of brittleness of disordered materials could in some ways be encoded in their energy landscape. To establish our conclusions, we simulate a selection of various disordered phases, namely: (i) calcium–silicate–hydrate (C–S–H) colloidal gels, (ii) silica (SiO<sub>2</sub>) glasses, (iii) amorphous silicon (a-Si) solids, and (iv) Cu<sub>64</sub>Zr<sub>36</sub> metallic glasses. These non-crystalline phases range over different families of disordered phases (gel, glass, and amorphous solid), scales (atomic networks and colloidal gels), and different types of bonds (Van der Waals, covalent, ionocovalent, and metallic)—which allows us to explore behaviors that are potentially generic to disordered materials. Based on molecular dynamics (MD) simulations, we show that the propensity for ductility during fracture increases

<sup>a</sup> State Key Laboratory of Water Resources and Hydropower Engineering Science, Wuhan University, Wuhan 430072, China. E-mail:zw\_mxx@whu.edu.cn

<sup>b</sup> Physics of Amorphous and Inorganic Solids Laboratory (PARISlab), Department of Civil and Environmental Engineering, University of California, Los Angeles, California 90095, USA. E-mail:bauchy@ucla.edu

<sup>c</sup> Key Lab of Structures Dynamic Behavior and Control of the Ministry of Education, Harbin Institute of Technology, Harbin 150090, China.

<sup>d</sup> Département de Physique and Regroupement Québécois sur les Matériaux de Pointe, Université de Montréal, Case Postale 6128, Succursale Centre-Ville, Montréal (QC), Canada H3C 3J7.

<sup>†</sup> Electronic Supplementary Information (ESI) available.

with the magnitude of structural disorder. To reveal the origin of this feature, we then adopt the activation-relaxation technique (ART), which enables a systematic search of saddle points and transition pathways in the energy landscape surface<sup>25</sup>. We establish that the propensity for ductility in disordered materials is encoded in the static topography of the energy landscape.

## 2 Results

### 2.1 Effect of disorder on brittleness and ductility

To explore the link between structural disorder and degree of ductility during fracture, we first consider a series of colloidal silicate gels (which consist of nanometric C–S–H grains that interact with each other via a generalized Lennard-Jones potential) and glassy silica ( $\text{SiO}_2$ ) samples exhibiting a wide range of degrees of disorder. To this end, starting from an initial crystalline structure, these systems are gradually amorphized by mimicking irradiation-introduced disordering (see Methods section). The overall degree of structural disorder is quantified by a two-body entropy term  $s$ , wherein lower values of  $s$  denote lower degrees of disorder (see Methods section).

We then investigate the fracture of the simulated disordered systems by subjecting them to a uniaxial tensile deformation (see Methods section). Fig. 1(a) shows the stress-strain curves of select colloidal gels systems upon uniaxial fracture. We observe that the most ordered systems (i.e., low  $s$ ) exhibit a fairly brittle response, which manifests itself by a sudden drop in stress after the crack starts to propagate. In contrast, the most disordered systems (i.e., high  $s$ ) feature a more ductile fracture, as evidenced by the slow decay of stress after the crack starts to propagate.

A similar phenomenon is also observed in the case of the glassy silica samples (see Fig. 1(b)). Specifically, we observe that, after reaching their maximum stress, highly disordered silica samples (i.e., high  $s$ ) exhibit a range of strains wherein the stress remains constant (i.e., yielding regime), which indicates the existence of plastic deformations. We note that, due to differences in spatial scales and in bonding nature (i.e., ionocovalent bonds for glassy silica vs. Van der Waals bonds for the colloidal gel), the silica glasses can reach significantly higher stress and strain values than the colloidal gels before failing. Nevertheless, despite the significantly different nature of these two systems, we observe that, interestingly, their respective degree of ductility exhibit a very similar dependence on the extent of structural disorder.

We then further quantify the extent of ductility by calculating the plastic energy  $G^P$  that is dissipated during fracture increases (see Methods section). We find that, in both systems,  $G^P$  increases fairly linearly with increasing degrees of disorder, as captured by the entropy term  $s$  (see the insets of Fig. 1). These results demonstrate that both of these disordered systems exhibit a DBT that is driven by the degree of structural disorder—wherein higher disorder results in higher ductility (lower brittleness).

### 2.2 Ductile events occurring during fracture

We now further investigate the nature of the carriers of plasticity within the network during fracture. To this end, we compute the cumulative non-affine displacement  $D$  of each atom/grain,

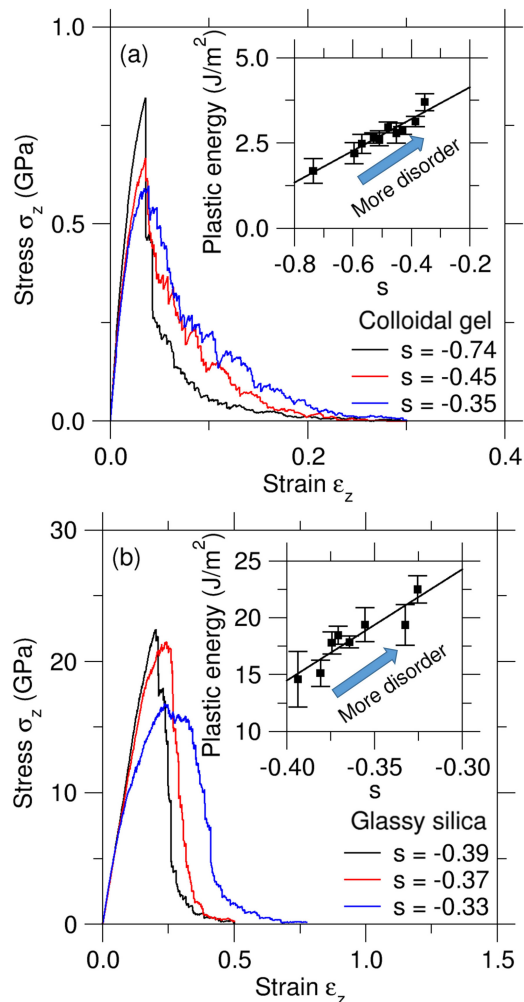


**Fig. 1** Stress-strain curves of select (a) colloidal gels and (b) silica glasses showing varying degrees of structural disorder (as captured by the entropy term  $s$ ) subjected to a uniaxial tensile deformation. The insets show the plastic energy dissipated during fracture as a function of  $s$ . The line is to guide the eye.

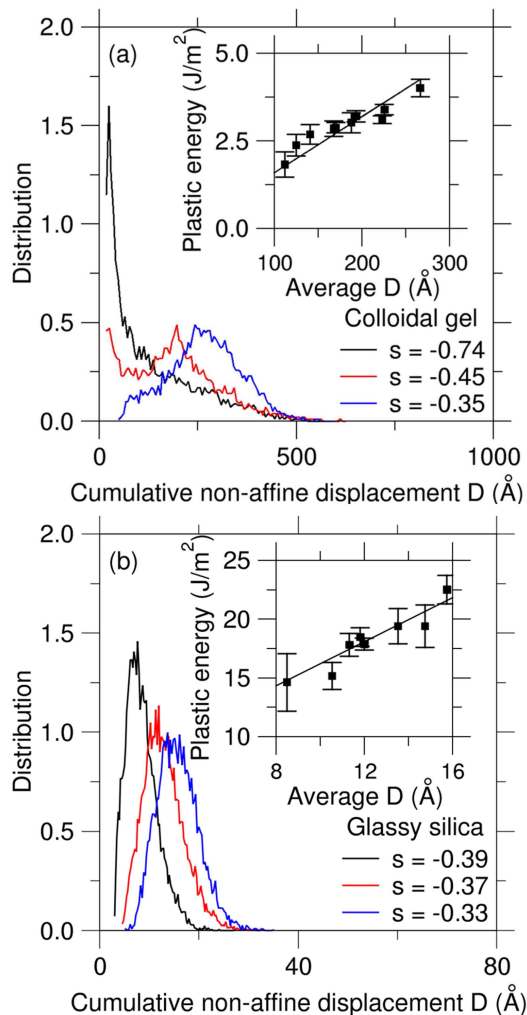


**Fig. 2** Distribution of the cumulative non-affine displacements  $D$  of the atoms (or particles) during the fracture of select (a) colloidal gels and (b) silica glasses with varying degrees of disorder (as captured by the entropy term  $s$ ). The inset shows the plastic energy dissipated during fracture as a function of the average value of  $D$  for varying degrees of disorder. The line is a linear fit.

which is used to identify the activation of STZs by capturing the irreversible structural reorganizations occurring during the fracture process (see Methods section). The distribution of the final cumulative non-affine displacement of the particles in select colloidal gels with varying degrees of disorder is shown in Fig. 2(a). We observe that, in the most ordered colloidal gel systems (i.e., low  $s$ ), most of the particles exhibit small values of  $D$  (lower than 2 times of their diameter). This indicates that, in this regime, most of the particles are displaced in an affine fashion, that is, the system exhibits a very limited extent of structural reorganization during fracture. In contrast, in more disordered colloidal gel systems (i.e., higher values of  $s$ ), the particles tend to exhibit larger  $D$  values (see Fig. 2(a)), which indicates that the extent of structural reorganization increases with increasing degree of disorder. A similar behavior is observed in the glassy silica samples (see Fig. 2(b)).

Interestingly, despite the different nature of these two systems,

we find that the extent of non-affine plastic deformations and resulting energy dissipation exhibit a similar relationship in both systems. As shown in the insets of Fig. 2, we find that, for both systems, the plastic energy  $G^P$  that is dissipated during fracture increases fairly linearly with the average final cumulative non-affine displacement  $D$ —i.e., as averaged over all the atoms (or particles) of fractured systems with fixed degrees of disorder. This strongly suggests that, during fracture, the magnitude of plastic energy dissipation (i.e., ductility) is indeed governed by the extent of non-affine reorganizations of the particles under stress. Overall, these results further support the ability of the non-affine displacement  $D$  to describe the carriers of plasticity within the network during fracture.

### 2.3 Effect of disorder on the topography of the energy landscape

We now explore how the link between degree of structural disorder, atoms/particles' dynamics under stress, and macroscopic degree of brittleness during fracture can be rationalized in terms of the topography of the underlying energy landscape of the system. To this end, we adopt activation-relaxation technique nouveau (ARTn, a method that is capable of computing the energy barriers of amorphous system without prior knowledge of the final state) to obtain the distribution of local energy barriers (see Methods section for more details). Fig. 3(a) shows the distribution of the energy barriers computed by ARTn for select colloidal gels with varying degrees of structural disorder. Overall, we find that the energy barrier distributions obtained herein strongly echo those previously computed in metallic glasses<sup>27</sup>. In detail, we observe that the more ordered colloidal gel systems (i.e., low  $s$ ) exhibit a series of fairly well-defined energy barriers around 250, 1000, and 1700 eV. This indicates the existence of a rough energy landscape, wherein the metastable equilibrium positions are separated from each other by some high-energy barriers. In contrast, in the more disordered colloidal gel systems (i.e., high  $s$ ), we observe that most of the high-energy barriers vanish and are replaced by low-energy barriers (i.e., less than 250 eV).

The glassy silica systems exhibit a similar behavior, namely, the energy barrier distributions tend to shift toward lower energy values disordering (see Fig. 3(b)). We find that, although a pristine silica glass would exhibit clearly distinct low- and high-energy barriers (i.e., low barriers associated with the flipping of O atoms and high barriers associated with the breakage of Si–O bonds), the present irradiated samples present a fairly continuous distribution of energy barriers due to the presence of coordination defects. It should be noted that the difference in the scale of the energy barriers that are accessible in the colloidal gels and silica glasses (i.e., eV for the silica glasses vs. keV for the colloidal gels) arises from the significantly different value of the typical interparticle energy in these systems—since the bonding energy between grains in the colloidal gels is notably higher than the binding energy between Si and O atoms in the silica glasses. However, this does not mean that, overall, colloidal gels are more cohesive than silica glasses—since, when normalized by their volume, the cohesion energy of colloidal gels is lower than that of silica glasses.

As a distinctive feature between the two systems considered herein, we observe that, in the case of the most disordered configurations (i.e., low  $s$ ), the colloidal gels exhibit a notable fraction of very low energy barriers (i.e., less than 100 eV), whereas such excess of low energy barriers (i.e., low as compared to the typical bond energy) is not observed in the silica glasses (see Fig. 3). The existence of such low energy barriers in the disordered colloidal gels may arise from the non-directional nature of the Van der Waals bonds—so that certain particles can rotate with respect to each other for a very low energy cost. This results in the appearance of some localized floppy modes of relaxation within the network. In contrast, the repulsive Coulombic interactions acting between cations (anions) in the silica glasses result in fairly well-defined interatomic angles and prevent any low-energy rotations of the atoms with respect to each other.

Although the energy barriers observed in the colloidal gels are significantly larger than in the silica glasses, such colloidal gels are associated with a larger length scale (i.e., larger interparticle distance). As such, taking into account the role the volume, the colloidal gels actually present a lower average volumetric density of energy barriers as compared to glassy silica—which explains the larger mobility of the particles in the gels. In turn, to compare the energy barriers observed in both systems to their fracture energy (or dissipated plastic energy), these energy barriers should be rescaled per unit of area—so as to obtain a surface density of energy that has the same unit as a fracture energy. We find that the colloidal gel and glassy silica systems exhibit a surface density of energy barriers that is around 0.25 and 1.6 eV/Å<sup>2</sup>, respectively, which echoes the fact that the colloidal gels tend to show lower fracture energies (or plastic energy) as compared to silica glasses.

Nevertheless, despite such differences, we observe that these two systems exhibit a similar type of scaling between disorder and landscape topography. Indeed, in both cases, we find that the average magnitude of the energy barriers decreases fairly linearly with increasing structural disorder, i.e., higher  $s$  values (see the insets in Fig. 3). This indicates that, in both cases, starting from an initially rough energy landscape in ordered configurations, disordering inducing a gradual smoothing of the energy landscape—that is, disordering results in a decrease in the average height of the saddle points separating the different metabasins accessible within the energy landscape.

#### 2.4 Effect of the energy landscape on ductility

We now investigate the nature of the link, if any, between the topography of the energy landscape and the propensity for disordered phases to activate ductile events upon fracture. To this end, Fig. 4(a) shows the cumulative non-affine displacements  $D$  of the particles during fracture as a function of the average height of the energy barriers  $E_{\text{ave}}$  that are accessible to them in select colloidal gels with varying degrees of structural disorder. For statistical averaging purposes, each of the data point shown in Fig. 4(a) corresponds to the averaging of  $D$  and  $E_{\text{ave}}$  over 5% of all the particles (as sorted in terms of increasing values of  $D$ ). Notably, we observe a clear (anti)correlation between the average height of

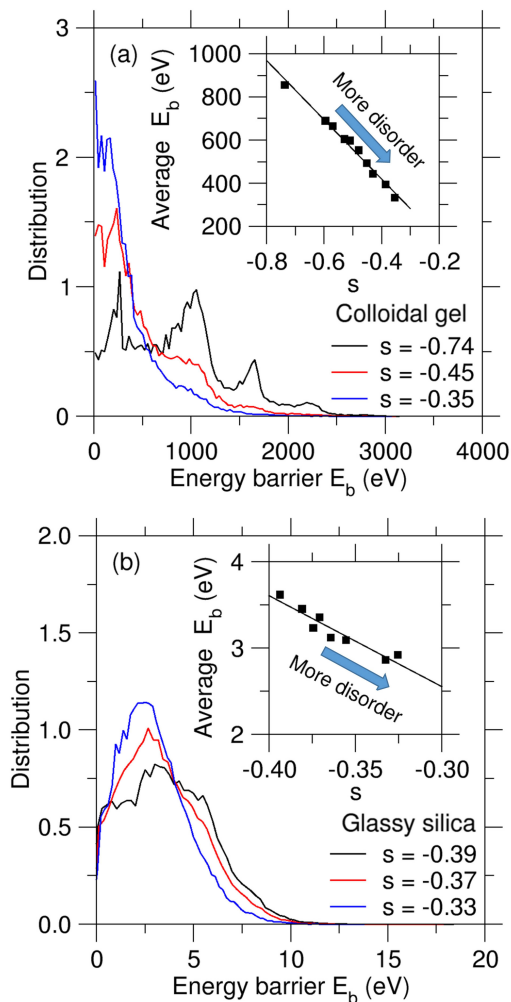


**Fig. 3** Distribution of the energy barriers in select (a) colloidal gels and (b) silica glasses with varying degrees of disorder (as captured by the entropy term  $s$ ). The inset shows the average value of the energy barriers as a function of  $s$ . The line is to guide the eye.

the energy barriers accessible to a particle and its non-affine displacement during fracture, namely, the particles that have access to low energy barriers are more likely to undergo some structural reorganization during fracture than those that only have access to large energy barriers. It should be noted that the monodisperse LJ colloidal gel considered is fairly unstable and tends to easily crystallize at non-zero temperature—so that this system is more "amorphous" than "glassy"<sup>28</sup>. Nevertheless, the crystallization time of this system depends on temperature (see Fig. S1 in Supplementary materials) and can become extremely long at low temperature. As such, the power law relationship evidenced herein still holds at non-zero temperature (see Fig. S3 in Supplementary materials).

We observe that, despite the difference in spatial and energy scale, the silica glasses exhibit a very similar behavior, namely, the non-affine displacement of a given atom during fracture decreases with increasing average height of the energy barriers that are accessible to this atom ( Fig. 4(b)). Interestingly, in both systems, our data suggest the existence of a power law relationship between the non-affine displacement  $D$  of the atoms (or particles) during fracture and the average height of the energy barriers  $E_{\text{ave}}$  they have access to:

$$D \propto AE_{\text{ave}}^{-\alpha} \quad (1)$$

where  $\alpha$  is a power law coefficient. However, we find here that the parameter  $\alpha$  is non-universal and appears to be system-specific. We also find, within a given system, the power law coefficient  $\alpha$  depends on the degree of disorder—albeit to a lesser extent for glassy silica (which may arise from the fact that this system exhibits a limited range of degrees of disorder  $s$ ). This suggests that the relationship between non-affine displacement and energy barriers may be governed by the fractal geometry of the energy landscape<sup>29</sup>. This aspect should be further investigated in future studies. It should be noted that the power law relationship identified herein is fundamentally different from the one reported in Ref.<sup>30</sup>, wherein the atomic displacement to reach the saddle point was noted to increase with activation energy (simply a consequence of the fact that the energy basin is fairly harmonic). In contrast, the power law identified herein (i.e., wherein non-affine displacement decreases with the local energy barrier) highlights that the overall dynamics of the particles upon fracture is encoded in the static topography of the energy landscape, that is, before any load is applied.

Furthermore, we also investigate whether the particle dynamics are governed by the minimum (rather than average) height of the energy barrier ( $E_{\text{min}}$ ) that are accessible to the particles. As show in Fig. S8, we find that the relationship between  $D$  and  $E_{\text{min}}$  can also be described by a power law. However, we observe that  $D$  exhibits a stronger correlation with  $E_{\text{ave}}$  than  $E_{\text{min}}$  (as measured from the coefficient of determination  $R^2$ ) for all of the systems considered in this study (see Supplementary Materials for more information). The fact that the dynamics of the particles is governed by the average (rather than minimum) height of the energy barriers they have access to can be understood from the fact that, during fracture, the dynamics of the particles are not

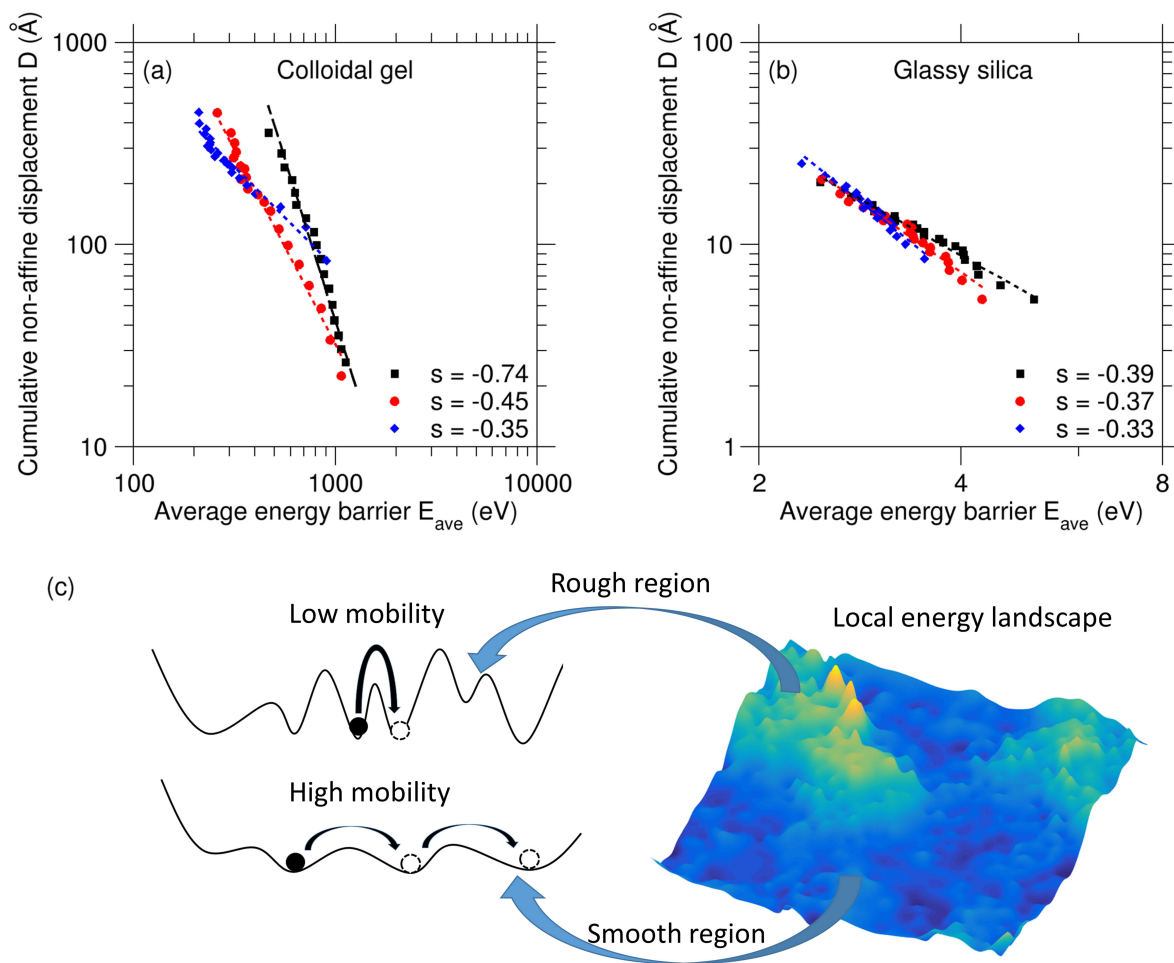
spontaneous, but actually driven by the application of an external load, along a certain fixed direction. Due to the directionality of the applied deformation, the particles are significantly more likely to reorganize along the direction of the deformation rather than simply by following paths associated with the lowest energy barriers (see Fig. S9).

Moreover, we find that atoms in silica glasses tend to exhibit two types of non-affine displacement: (i) very small displacements that are well below 0.1 Å and (ii) more significant displacements (i.e., around 1-to-6 Å). We observe that only the largest displacements are associated with notable drops in stress and, hence, contribute to any significant energy dissipation (and, hence, ductility) upon fracture (see Fig. S10 in Supplementary Material). As shown in Fig. S10, ARTn can properly capture the energy barriers that are associated with notable atomic displacements (ranging from 0.5-to-6 Å), which contribute to increasing ductility.

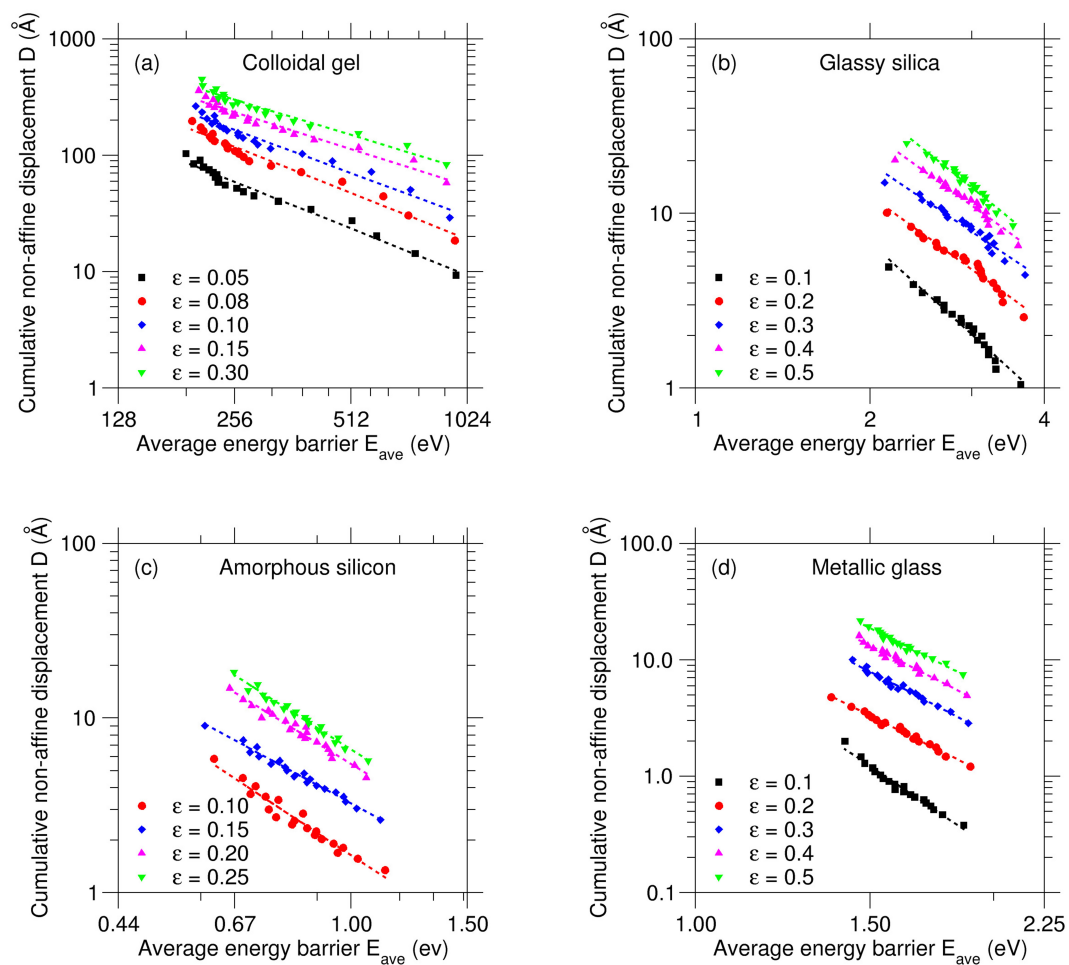
We now discuss the degree of generality of the link evidenced herein between energy landscape topography, particles' dynamics under stress, and macroscopic ductility during fracture. Specifically, we explore whether the power law relationship between the non-affine displacement  $D$  of the particles during fracture and the average height of the energy barriers  $E_{\text{ave}}$  they have access to could be a generic feature of disordered phases. To this end, we extend our analysis to two additional classes of disordered materials, namely, a-Si (an archetypical covalent amorphous solid) and Cu<sub>64</sub>Zr<sub>36</sub> (an archetypal metallic glass). The above two disordered materials are generated by the conventional melting-cooling method (see Method section for more details).

Fig. 5 shows the cumulative non-affine displacements  $D$  of the atoms/particles after varying strains as a function of the average height of the energy barriers  $E_{\text{ave}}$  that are accessible to them in each of the four systems considered herein (at the fixed degree of disorder). Quite unexpectedly, despite the notable difference in spatial scale (from Å to 100s of nm), energy scale (from eV to keV), and bonding (Van der Waals, covalent, ionocovalent, and metallic), a similar power law relationship is observed in all these systems. In addition, it is notable that the power law relationship remains satisfied for varying strain deformations, both before and after fracture (as long as the deformation is large enough to induce some atomic motion). We find that the power law coefficient  $\alpha$  remains largely unaffected by the magnitude of the applied strain. This indicates that, despite the atomic reorganizations occurring during the deformation, the system remains close to its initial position in the energy landscape and the atoms retain the memory of the topography of their local initial energy landscape.

It should be noted that the characteristic length scale of colloidal gels (interparticle distance of 50 Å) is much larger than the characteristic length scale of silica glass (interparticle distance of 1-to-2 Å). As a consequence, although the energy barriers observed in the colloidal gel are, on average, significantly larger than in glassy silica, the volumetric density of energy barriers in colloidal gels is, in turn, lower than in glassy silica (see Fig. S5 in Supplementary materials). This explains why particles tend to exhibit higher mobility in the colloidal gel.



**Fig. 4** Cumulative non-affine displacements  $D$  of the atoms (or particles) during fracture as a function of the average height of the energy barriers that are accessible to them. The data are presented for select (a) colloidal gels and (b) silica glasses with varying degrees of disorder (as captured by the entropy term  $s$ ). (c) Schematic illustrating how the topography of the energy landscape controls the propensity for atoms (or particles) to reorganize in a non-affine fashion during fracture. The initial and final metastable equilibrium positions of the particles in the energy landscape are indicated in black and white, respectively. Rough regions of the energy landscape are characterized by large energy barriers separating each metabasin, whereas smooth regions comprise energy metabasins that are separated from each other by small energy barriers.



**Fig. 5** Cumulative non-affine displacements  $D$  of the atoms (or particles) during fracture as a function of the average height of the energy barriers that are accessible to them. The data are presented for a (a) colloidal gel, (b) silica glass, (c) amorphous silicon, (d) and  $\text{Cu}_{64}\text{Zr}_{36}$  metallic glass subjected to varying strains  $\varepsilon$ .

Disordered materials (e.g., irradiated or melt-quenched phases) are out of equilibrium and, hence, their mechanical properties depend on their history. However, we find that (i) the relationship between plastic energy and non-affine particle displacement and (ii) the power law relationship between  $D$  and  $E_{ave}$  are independent on whether disorder is introduced via irradiation or melt-quenching (see Supplementary Materials). This suggests that the fact that the ductility of disordered systems is quantitatively encoded in their static energy landscape is a generic feature of disordered materials—independently of how structural disorder is induced.

### 3 Conclusions

Overall, our results suggest the following atomic picture of ductility in non-crystalline materials. Under load, the particles gain some elastic strain energy, which effectively deforms the local energy landscape. In highly disordered/unstable systems, this elastic energy becomes comparable to the height of the barriers in the energy landscape—so that the particles can overcome some of the energy barriers and reorganize (see Fig. 4(c)). These structural reorganizations correspond to some plastic events that allow the system to release some of the accumulated internal stress and, thereby, reach higher strain deformations while resisting fracture (see Fig. 4). In contrast, in less disordered systems, the elastic energy provided to the particles remains low as compared to the height of most of the energy barriers that are accessible to the particles—due to the high roughness of the energy landscape. As such, the particles remain trapped in their metabasins and the structure remains fairly frozen under load (i.e., with no significant plastic structural reorganization) until the elastic energy becomes equal to the surface energy—the point at which the system eventually fails in a brittle fashion. In that regard, it is notable that, even when significant deformations and structural reorganizations occur, the dynamics of the particles remains largely correlated to the initial height of the energy barriers. This highlights the existence of a close relationship between long-time dynamics and the topography of the static energy landscape (before any load is applied), which is herein observed for a large variety of materials. However, this ductile behavior is qualitatively different from the ductility exhibited by some metals, where macroscopic shear bands are expected to be observed. It should be pointed out that the role of structural defects on ductility identified herein would not apply to pristine crystalline materials that can exhibit slip deformations—since, in this case, the introduction of structural disorder would limit ductility by suppressing preexisting shearing mechanisms.

Altogether, these results establish a consistent atomic picture of ductility in various families of disordered materials (i.e., colloidal gel, ionocovalent glass, covalent amorphous solid, and metallic glass) and highlight the critical role played by the topography of the energy landscape in controlling the degree of brittleness in disordered materials<sup>31,32</sup>. The large similarity of the behaviors observed herein for a wide variety of material families suggests that the relationship between energy landscape topography and ductility during fracture might be a generic feature of disordered materials<sup>8,9,33–35</sup>. We envision that the present results

could guide the design of novel non-crystalline phases with unusual resistance to fracture.

## 4 Methods

### 4.1 Construction of the disordered phases

We simulate a selection of various disordered phases, namely: (i) C–S–H colloidal gels, (ii) SiO<sub>2</sub> glasses, (iii) a-Si solids, and (iv) Cu<sub>64</sub>Zr<sub>36</sub> metallic glasses by using the LAMMPS package<sup>36</sup>, as detailed in the following.

*Colloidal gel:* We first consider the C–S–H colloidal gel model developed by Masoero *et al.*<sup>33</sup>. This system consists of nanometric C–S–H grains that interact with each other via a generalized Lennard-Jones (LJ) potential:

$$U_{ij} = 4\epsilon \left[ \left( \frac{\sigma}{r_{ij}} \right)^{\gamma_{rep}} - \left( \frac{\sigma}{r_{ij}} \right)^{\gamma_{att}} \right] \quad (2)$$

where  $r_{ij}$  is the distance between each pair of grains. Following Masoero's model<sup>33</sup>, we use  $\gamma_{rep} = 28$  and  $\gamma_{att} = 14$  (to describe the repulsive and attractive energy terms, respectively),  $\epsilon = 115.38$  eV, and  $\sigma = 50$  Å. The distance cutoff is fixed at 100 Å. These parameters have been shown to properly describe the nanomechanics of C–S–H gels<sup>33,37–39</sup>. The C–S–H models simulated herein comprises 8000 grains in a cubic box of around 1000 Å. The initial configuration takes the form of a DNA-like lattice (see Ref.<sup>39</sup> for more details about the simulated system).

*Glassy silica:* We then consider glassy SiO<sub>2</sub>, i.e., an archetypical ionocovalent oxide glass. To this end, we adopt the well-established van Beest-Kramer-van Santen (BKS) potential, which offers a representation of the structure of SiO<sub>2</sub> while relying on a simple 2-body Buckingham formulation:

$$U_{ij} = \frac{q_i q_j}{r_{ij}} + A_{ij} \exp(-b_{ij} r_{ij}) - \frac{c_{ij}}{r_{ij}^6} \quad (3)$$

where  $A_{ij}$ ,  $b_{ij}$ ,  $c_{ij}$ , and  $q_i$  are potential parameters<sup>40</sup>. To avoid the "Buckingham catastrophe," an additional repulsive term is added at very short distance following Ref.<sup>41</sup>. The cutoff is fixed at 10 Å. The SiO<sub>2</sub> models simulated herein comprises 8640 atoms. We use a  $\alpha$ -quartz crystal as initial configuration.

*Disordering:* To investigate the effect of disorder, the previous two crystalline systems (i.e., C–S–H and  $\alpha$ -quartz) are gradually amorphized by simulated irradiation, which reproduce the irradiation-induced disordering of solids observed experimentally<sup>26,42,43</sup>. In detail, a particle (grain or atom) is first randomly selected. Its kinetic energy is then instantaneously increased by an increment  $\Delta E_K$  ( $\Delta E_K = 40$  keV and 2 keV for C–S–H and SiO<sub>2</sub>, respectively). The kinetic energy deposition results in a ballistic cascade within a region of the network. To avoid any spurious effects of the thermostat on the dynamics of the ballistic cascade, we define a sphere around the primary knocked-on atom, wherein the dynamics of the atoms is simulated in the *NVE* ensemble, while the dynamics of the rest of the atoms is simulated in the *NVT* ensemble under 300 K with a Nosé-Hoover thermostat<sup>44,45</sup>. The radius of the spherical region is fixed at 5 times the radius of the first coordination shell (taken as the position of the first minimum in the pair distribution function). We find that

relaxation durations  $\Delta t$  of 200 ps and 20 ps for C–S–H and SiO<sub>2</sub>, respectively, are long enough to ensure convergence of temperature, energy, and pressure. Note that, to avoid any unrealistic atom overlapping upon high-energy collision, a variable timestep is used during this stage. Otherwise, we use a constant timestep of 5 fs and 1 fs for C–S–H and SiO<sub>2</sub>, respectively. After each ballistic cascade, the system is then further relaxed in the *NPT* ensemble under 300 K and zero pressure for the same duration  $\Delta t$ , which is long enough to ensure a convergence of the volume. This process is then iteratively repeated until saturation<sup>26</sup>. For each system, we subsequently extract a series of configurations featuring various degrees of disordering for further characterization. Note that only systems having undergone at least 40 ballistic cascades are selected—which was found appropriate to exclude the existence of any residual crystalline order in the simulated systems.

**Metallic glass:** In addition to the two previous systems, we consider a Cu<sub>64</sub>Zr<sub>36</sub> glass with a fixed degree of disorder. This system allows us to assess whether our conclusions (see below) apply to metallic glasses. We adopt the embedded-atom method potential parameterized by Mendelev *et al.*, which has been shown to give a reasonable description of the structure and elastic behavior of Cu–Zr glass<sup>46</sup>. An initiation configuration is first created by randomly placing 8000 atoms in a cubic box while ensuring the absence of any unrealistic overlap. The system is then equilibrated at 2000 K under zero pressure for 10 ns in the *NPT* ensemble to lose the memory of its initial configuration. The melt is then subsequently cooled down to 300 K with a cooling rate of 1 K/ps under zero pressure in the *NPT* ensemble. Finally, the obtained glass is relaxed at 300 K and under zero pressure for an additional 10 ns.

**Amorphous silicon:** Finally, we consider an amorphous Si model (i.e., an archetypical model for disordered covalent semiconductors) with a fixed degree of disorder. To this end, we adopt the 3-body Stillinger-Weber potential, which has been shown to reproduce the vibrational and structural properties in agreement with experiments<sup>47</sup>. A disordered system comprising 8000 atoms is prepared using the same melt-quench method as that used for Cu<sub>64</sub>Zr<sub>36</sub>.

## 4.2 Degree of disorder

To quantify the degree of disorder in each configuration, we compute a 2-body entropy  $s$  based on the pair distribution function  $g(r)$  as<sup>48,49</sup>:

$$s = -\frac{1}{R} \int [g(r) \ln g(r) - (g(r) - 1)] dr \quad (4)$$

where  $R$  is the distance cutoff. Note that this entropy term  $s$  would be equal to 0 if  $g(r) = 1$  (i.e., for a perfectly disordered gas), whereas lower values of  $s$  (i.e., negative values of  $s$ ) denote a lower degree of disorder. For illustration purposes, we also calculate the local structural order of each atom  $i$  as:  $s_i = -\frac{1}{R} \int [g_i(r) \ln g_i(r) - (g_i(r) - 1)] dr$ , where  $g_i(r)$  is the local pair distribution characterizing the radial order around each atom

*i*. As illustrated in Fig. 6, we observe that, both for C–S–H and SiO<sub>2</sub>, the degree of disorder increases upon irradiation.

## 4.3 Fracture simulations

The fracture of the simulated disordered systems is performed by subjecting them to a uniaxial tensile deformation. This is achieved by deforming each system along the  $z$ -axis by small increments of a strain of 0.05% while keeping the size of the simulation box fixed along the other directions and performing an energy minimization (using the conjugate gradient algorithm) at each step of the deformation. This procedure is iteratively repeated until the system breaks (as illustrated in Fig. S1 in Supplementary materials). For each configuration, the fracture is repeated along the  $x$ - and  $y$ -axis for statistical averaging. We compute the undergone uniaxial stress as a function of strain to characterize the response of each system upon fracture. We then compute the fracture energy  $G_C$  from the integral of the stress-strain curve (i.e., the energy work associated with the fracture process)<sup>50</sup>. The cohesion of the system is then estimated by computing its surface energy  $\gamma$  by cutting the system into two parts (i.e., creating two free surfaces), relaxing the as-cut system for  $\Delta t$  in the *NPT* ensemble, and computing the loss of potential energy with respect to that of bulk system<sup>50</sup>. Note that the  $\gamma$  values are calculated for 300 cut surfaces (100 per axis) for statistical averaging. The value of the surface energy  $\gamma$  is here found to be fairly unaffected by the degree of disorder (not shown).

The degree of brittleness of fracture can then be quantified by calculating the irreversible plastic energy  $G^P$  that is dissipated during fracture by decomposing the elastic and non-elastic energy terms contributing to the total fracture energy<sup>50</sup>:

$$G_C = 2\gamma + G^P \quad (5)$$

The plastic energy  $G^P$  that is dissipated during fracture is then calculated as  $G_C - 2\gamma$ , that is, it corresponds to the amount of fracture energy that is not consumed to create a new surface. Note that  $G^P = 0$  denotes a fully brittle fracture, that is, wherein all the fracture energy is consumed to create some new surface.

In contrast to what is observed with the other systems considered herein, we find that a uniaxial tensile deformation does not yield any fracture via crack propagation in Cu<sub>64</sub>Zr<sub>36</sub>. Hence, to assess the ductility of this system, we subject this configuration to an athermal quasistatic shear (AQS) deformation with Lees-Edwards periodic boundary conditions<sup>19,23,51</sup>.

## 4.4 Cumulative non-affine displacement

To investigate the nature of the plastic events occurring within the network during fracture, we compute the cumulative non-affine displacement  $D$  undergone by each particle during the entire fracture process. The non-affine square displacement  $D_{\min}^2$  metric has been widely used to identify the activation of STZs under stress<sup>20,51,52</sup>. The main idea of the non-affine displacement is to isolate the particle displacements associated with local reorganizations from the displacements resulting from the macro-

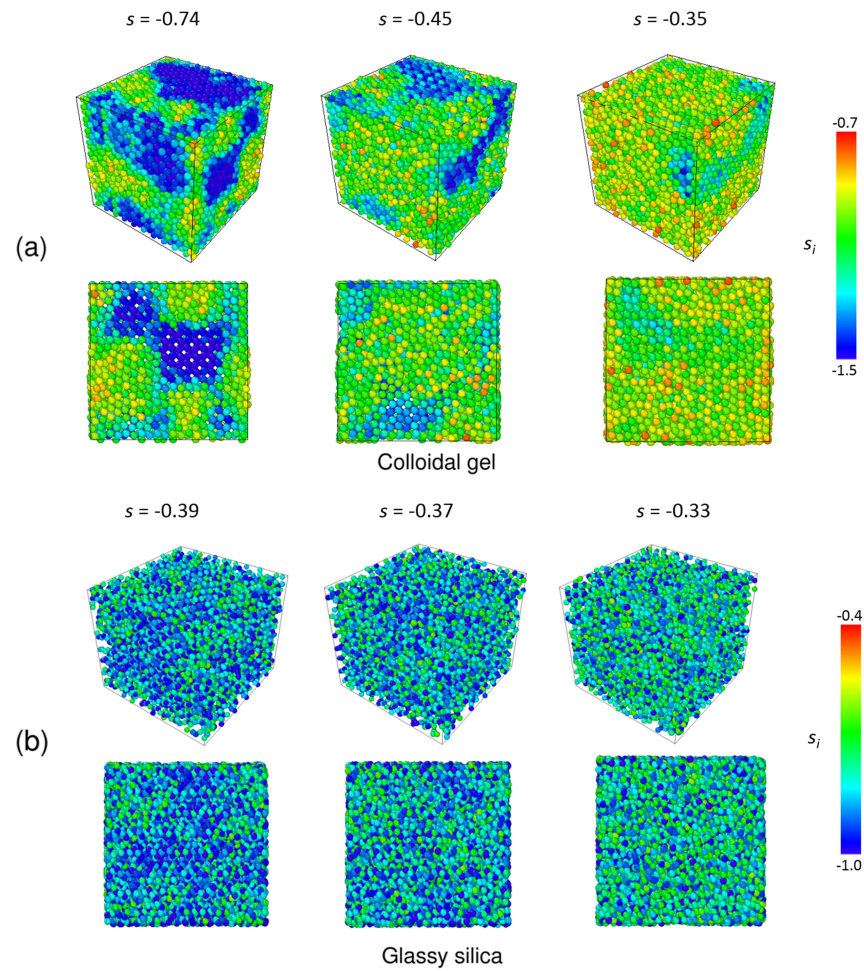


**Fig. 6** Snapshots of select (a) colloidal gels and (b) silica glasses with varying degrees of disorder. Each atom is colored based on its local excess entropy  $s_i$ .

scopic deformation of the simulation box. It provides a quantitative measurement of the degree of local reorganizations that atoms have undergone when comparing two consecutive configurations. Here, rather than relying on the total non-affine displacement during fracture—which is not a meaningful metric since the configuration experiences some significant changes upon fracture—we rely on a cumulative non-affine displacement  $D$ , which is defined, for each particle, as the sum of the non-affine displacements experienced during each small increment of strain:

$$D = \sum_{i=1}^n \sqrt{\Delta D_{i,\min}^2} \quad (6)$$

where  $\Delta D_{i,\min}^2$  is the incremental non-affine square displacement after each small increment of strain  $i$  and  $n$  is the total number of the strain increments. Local cutoff values of 60 Å, 3.38 Å, 2.9 Å, and 3.7 Å are selected to compute the local affine displacement field for the silicate gels, glassy silica, amorphous silicon, and Cu<sub>64</sub>Zr<sub>36</sub> glass, respectively.

#### 4.5 Exploring the local energy landscape

Finally, we explore whether the ductility of the disordered phases considered herein could in some ways be encoded in the topography of the energy landscape. To this end, we adopt the activation-relaxation technique nouveau (ARTn) method<sup>25,53,54</sup>, which has been previously used to compute the energy barrier distribution in disordered materials<sup>23,27,30,55</sup>. In details, starting from a local minimum in the energy landscape, random displacements are imposed on a select particle and its neighbors to identify a direction of negative curvature in the energy landscape, which is indicative of the presence of a nearby first-order saddle point. Here, the radius of the local region that is initially deformed is chosen as being equal to the cutoff radius used for the calculation of the non-affine displacements (see above). The system is then moved to the saddle point by following the direction of negative curvature using the Lanczos algorithm<sup>25</sup> before the system eventually relaxes toward a new minimum. Hence, the ARTs algorithm restricts its search of energy pathways to those going through saddle points and, thereby, focuses on the minuscule fraction of the configurational space that is physically accessible to the system. We adopt here force tolerance values of 0.1 eV Å<sup>-1</sup>, 0.05 eV Å<sup>-1</sup>, 0.01 eV Å<sup>-1</sup>, and 0.05 eV Å<sup>-1</sup> for the convergence of the saddle points in the silicate gels, glassy silica, amorphous silicon, and Cu<sub>64</sub>Zr<sub>36</sub> glass, respectively. A total of 20 saddle point searches is conducted for each particle, which was here found to be large enough to ensure the convergence of the energy barrier distribution.

#### Conflicts of interest

The authors declare no competing financial interests.

#### Acknowledgements

This work was supported by the National Key R&D Program of China (Grant No. 2017YFC0404801), the National Science Fund for Distinguished Young Scholars (Grant No. 51825905), and

the National Natural Science Foundation of China (Grant No. 51879206). Part of this work was also supported by the National Science Foundation under Grants No. 1762292 and 1922167. Part of the numerical calculations presented in this paper have been conducted on the supercomputing system in the Supercomputing Center of Wuhan University.

#### Notes and references

- 1 M. L. Falk and J. Langer, *Annual Review of Condensed Matter Physics*, 2011, **2**, 353–373.
- 2 A. Nicolas, E. E. Ferrero, K. Martens and J.-L. Barrat, *Rev. Mod. Phys.*, 2018, **90**, 045006.
- 3 B. A. Sun and W. H. Wang, *Progress in Materials Science*, 2015, **74**, 211–307.
- 4 A. Pineau, A. A. Benzerga and T. Pardoen, *Acta Materialia*, 2016, **107**, 424–483.
- 5 X. K. Xi, D. Q. Zhao, M. X. Pan, W. H. Wang, Y. Wu and J. J. Lewandowski, *Phys. Rev. Lett.*, 2005, **94**, 125510.
- 6 J. J. Lewandowski \*, W. H. Wang and A. L. Greer, *Philosophical Magazine Letters*, 2005, **85**, 77–87.
- 7 J. Schroers and W. L. Johnson, *Phys. Rev. Lett.*, 2004, **93**, 255506.
- 8 J. Ketkaew, W. Chen, H. Wang, A. Datye, M. Fan, G. Pereira, U. D. Schwarz, Z. Liu, R. Yamada, W. Dmowski, M. D. Shattuck, C. S. O'Shern, T. Egami, E. Bouchbinder and J. Schroers, *Nat Commun*, 2018, **9**, 1–7.
- 9 W. Li, Y. Gao and H. Bei, *Scientific Reports*, 2015, **5**, 14786.
- 10 G. Li, M. Q. Jiang, F. Jiang, L. He and J. Sun, *Materials Science and Engineering: A*, 2015, **625**, 393–402.
- 11 M. C. Li, M. Q. Jiang, G. Li, L. He, J. Sun and F. Jiang, *Intermetallics*, 2016, **77**, 34–40.
- 12 H. Schuler, C. Mayrhofer and K. Thoma, *International Journal of Impact Engineering*, 2006, **32**, 1635–1650.
- 13 J. R. Rice and R. Thomson, *The Philosophical Magazine: A Journal of Theoretical Experimental and Applied Physics*, 1974, **29**, 73–97.
- 14 Y. Q. Cheng and E. Ma, *Progress in Materials Science*, 2011, **56**, 379–473.
- 15 H. Jia, G. Wang, S. Chen, Y. Gao, W. Li and P. K. Liaw, *Progress in Materials Science*, 2018, **98**, 168–248.
- 16 M. Popovic, T. W. J. de Geus and M. Wyart, *Phys. Rev. E*, 2018, **98**, 040901.
- 17 D. Tüzes, P. D. Ispánovity and M. Zaiser, *Int J Fract*, 2017, **205**, 139–150.
- 18 B. Wang, Y. Yu, M. Wang, J. C. Mauro and M. Bauchy, *Phys. Rev. B*, 2016, **93**, 064202.
- 19 J. Ding, S. Patinet, M. L. Falk, Y. Cheng and E. Ma, *PNAS*, 2014, **111**, 14052–14056.
- 20 E. D. Cubuk, R. J. S. Ivancic, S. S. Schoenholz, D. J. Strickland, A. Basu, Z. S. Davidson, J. Fontaine, J. L. Hor, Y.-R. Huang, Y. Jiang, N. C. Keim, K. D. Koshigan, J. A. Lefever, T. Liu, X.-G. Ma, D. J. Magagnosc, E. Morrow, C. P. Ortiz, J. M. Rieser, A. Shavit, T. Still, Y. Xu, Y. Zhang, K. N. Nordstrom, P. E. Arratia, R. W. Carpick, D. J. Durian, Z. Fakhraai, D. J. Jerolmack,

- D. Lee, J. Li, R. Riggleman, K. T. Turner, A. G. Yodh, D. S. Gianola and A. J. Liu, *Science*, 2017, **358**, 1033–1037.
- 21 S. Patinet, D. Vandembroucq and M. L. Falk, *Phys. Rev. Lett.*, 2016, **117**, 045501.
- 22 Y. Cao, J. Li, B. Kou, C. Xia, Z. Li, R. Chen, H. Xie, T. Xiao, W. Kob, L. Hong, J. Zhang and Y. Wang, *Nature Communications*, 2018, **9**, 2911.
- 23 B. Xu, M. L. Falk, J. Li and L. Kong, *Phys. Rev. Lett.*, 2018, **120**, 125503.
- 24 M. Blank-Burian and A. Heuer, *Physical Review E*, 2018, **98**, 033002.
- 25 G. T. Barkema and N. Mousseau, *Phys. Rev. Lett.*, 1996, **77**, 4358–4361.
- 26 N. A. Krishnan, B. Wang, Y. Yu, Y. Le Pape, G. Sant and M. Bauchy, *Phys. Rev. X*, 2017, **7**, 031019.
- 27 Y. Fan, T. Iwashita and T. Egami, *Nature Communications*, 2017, **8**, 15417.
- 28 E. D. Zanotto and J. C. Mauro, *Journal of Non-Crystalline Solids*, 2017, **471**, 490–495.
- 29 H. J. Hwang, R. A. Riggleman and J. C. Crocker, *Nature Materials*, 2016, **15**, 1031–1036.
- 30 Y. Fan, T. Iwashita and T. Egami, *Nature Communications*, 2014, **5**, 5083.
- 31 G. Gagnon, J. Patton and D. J. Lacks, *Phys. Rev. E*, 2001, **64**, 051508.
- 32 C. E. Maloney and D. J. Lacks, *Phys. Rev. E*, 2006, **73**, 061106.
- 33 E. Masoero, E. Del Gado, R. J.-M. Pellenq, F.-J. Ulm and S. Yip, *Phys. Rev. Lett.*, 2012, **109**, 155503.
- 34 A. Ninarello, L. Berthier and D. Coslovich, *Phys. Rev. X*, 2017, **7**, 021039.
- 35 M. Ozawa, L. Berthier, G. Biroli, A. Rosso and G. Tarjus, *PNAS*, 2018, **115**, 6656–6661.
- 36 S. Plimpton, *Journal of Computational Physics*, 1995, **117**, 1–19.
- 37 H. Liu, S. Dong, L. Tang, N. M. Anoop Krishnan, E. Masoero, G. Sant and M. Bauchy, *Journal of Colloid and Interface Science*, 2019, **542**, 339–346.
- 38 H. Liu, L. Tang, N. M. A. Krishnan, G. Sant and M. Bauchy, *J. Phys. D: Appl. Phys.*, 2019, **52**, 315301.
- 39 H. Liu, S. Dong, L. Tang, N. M. A. Krishnan, G. Sant and M. Bauchy, *Journal of the Mechanics and Physics of Solids*, 2019, **122**, 555–565.
- 40 B. W. H. van Beest, G. J. Kramer and R. A. van Santen, *Phys. Rev. Lett.*, 1990, **64**, 1955–1958.
- 41 K. Vollmayr, W. Kob and K. Binder, *Phys. Rev. B*, 1996, **54**, 15808–15827.
- 42 N. M. A. Krishnan, Y. Le Pape, G. Sant and M. Bauchy, *Journal of Nuclear Materials*, 2018, **512**, 126–136.
- 43 N. M. A. Krishnan, B. Wang, G. Sant, J. C. Phillips and M. Bauchy, *ACS Appl. Mater. Interfaces*, 2017, **9**, 32377–32385.
- 44 S. Nosé, *J. Chem. Phys.*, 1984, **81**, 511–519.
- 45 W. G. Hoover, *Phys. Rev. A*, 1985, **31**, 1695–1697.
- 46 M. I. Mendeleev, M. J. Kramer, R. T. Ott, D. J. Sordelet, D. Yagodin and P. Popel, *Philosophical Magazine*, 2009, **89**, 967–987.
- 47 R. L. C. Vink, G. T. Barkema, W. F. van der Weg and N. Mousseau, *Journal of Non-Crystalline Solids*, 2001, **282**, 248–255.
- 48 A. Baranyai and D. J. Evans, *Phys. Rev. A*, 1989, **40**, 3817–3822.
- 49 M. Bauchy, B. Guillot, M. Micoulaut and N. Sator, *Chemical Geology*, 2013, **346**, 47–56.
- 50 M. Bauchy, B. Wang, M. Wang, Y. Yu, M. J. Abdolhosseini Qomi, M. M. Smedskjaer, C. Bichara, F.-J. Ulm and R. Pellenq, *Acta Materialia*, 2016, **121**, 234–239.
- 51 C. E. Maloney and A. Lemaître, *Phys. Rev. E*, 2006, **74**, 016118.
- 52 M. L. Falk and J. S. Langer, *Phys. Rev. E*, 1998, **57**, 7192–7205.
- 53 E. Cancès, F. Legoll, M.-C. Marinica, K. Minoukadeh and F. Willaime, *J. Chem. Phys.*, 2009, **130**, 114711.
- 54 R. Malek and N. Mousseau, *Phys. Rev. E*, 2000, **62**, 7723–7728.
- 55 H. Kallel, N. Mousseau and F. Schiettekatte, *Phys. Rev. Lett.*, 2010, **105**, 045503.